ACS APPLIED MATERIALS & INTERFACES

Research Article

www.acsami.org

Development of Nonstoichiometric $CuInS_2$ as a Light-Harvesting Photoanode and Catalytic Photocathode in a Sensitized Solar Cell

Jia-Yaw Chang,* Shueh Chien Chang, Shin-Hwa Tzing, and Chen-Hei Li

Department of Chemical Engineering, National Taiwan University of Science and Technology, Taipei City, Taiwan

Supporting Information

ABSTRACT: A simple one-pot approach was developed to obtain nonstoichiometric $CuInS_2$ nanocrystals. Using this approach, both In-rich and Cu-rich $CuInS_2$ nanocrystals could be reliably synthesized by tuning stoichiometric combinations of [Cu]/[In] precursor constituents. By designing Cu-rich $CuInS_2$ heteronanostructures to serve as counter electrodes, quantum-dot-sensitized solar cells (QDSSCs) equipped with In-rich $CuInS_2$ and CdS cosensitizers delivered a power conversion efficiency of 2.37%, which is significantly more efficient than conventional Pt counter electrodes. To the best of our knowledge, this study represents the first report utilizing nonstoichiometric $CuInS_2$ nanocrystals as a photon-harvesting sensitizer comprised of a photoanode and photocathode in QDSSCs; also unique to this report, these nonstoichiometric $CuInS_2$ nanocrystals were formed by simply changing the cationic molar ratios without complicated precursor preparation. Impedance spectroscopy and Tafel polarization indicated that these Cu-rich $CuInS_2$ heteronanostructures had electrocatalytic activities (used for reducing S^{2-}/S_n^{2-}) that were superior to a Pt catalyst. Moreover, we demonstrated that Cu-rich $CuInS_2$ heteronanostructures were also useful counter electrodes in dye-sensitized solar cells, and this finding revealed a promising conversion efficiency of 6.11%, which was ~96% of the efficiency in a cell with a Pt-based counter electrode (6.32%).

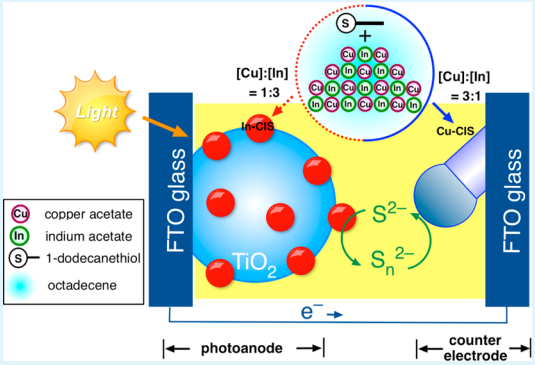

KEYWORDS: *quantum dots-sensitized solar cells, $CuInS_2$, nonstoichiometric ratio, light−harvesting sensitizer, counter electrode*

1. INTRODUCTION

Increasing global demand for energy has driven widespread development of affordable and environmentally sustainable energy resources. The utilization of solar radiation as a sustainable energy source is considered to be one of the most promising options to satisfy the global need for renewable energy. In recent years, quantum-dot-sensitized solar cells (QDSSCs) have gained increasing attention as a promising option for next-generation solar cells because of the quantum confinement effect, their large dipole moment, their high molar coefficients, and their multiple-exciton generation (MEG). In particular, the recent discovery of efficient MEG[1−3] (the relaxation of photoexcited carriers, which is induced by impact ionization) could be exploited to overcome the Shockley−Queisser limit (~31%)[4] and could, thereby, improve the performance of solar cells.[5] Accordingly, enormous efforts have been expended to use metal chalcogenides, such as CdS(Se),[6−9] PbS(Se),[10,11] $SnSe_2$,[12] and Sb_2S_3,[13] as light-harvesting sensitizers in QDSSCs. To achieve eco-friendly processes that avoid the use of toxic chemicals in preparative protocols, I−III−VI chalcopyrite semiconductor nanocrystals (SCs), such as $CuInS_2$, have attracted much attention in recent years to serve as Cd-free light-harvesting materials in QDSSCs because of their high extinction coefficients of ~10^5 cm^{-1} (at λ = 500 nm), their lack of highly toxic elements, and their suitable direct band gap (1.53 eV), which is well-matched to the optimal spectral range of a solar cell. Some successful approaches for preparing $CuInS_2$-based QDSSCs have been reported.[14−19]

Moreover, to develop QDSSCs with high efficiencies, in addition to the careful selection of light-harvesting sensitizers, another equally crucial component of QDSSCs is their counter electrode (CE), which enables the transfer of electrons from the external circuit back to the electrolyte and catalyzes the reduction of the redox electrolyte. However, the conventional platinized CE, which is widely used in dye-sensitized solar cells (DSSCs), exhibits poor catalytic activity in the S^{2-}/S_n^{2-} redox electrolyte because of the adsorption of S atoms,[20] which results in a bottleneck in the electron flow. Therefore, it is imperative to develop alternative materials to serve as CEs in QDSSCs. Attractive candidates for CEs in QDSSCs, Cu-based nanomaterials (such as Cu_2S, Cu_2SnS_3, and Cu_2ZnSnS_4) exhibit outstanding electrochemical properties.[21−26] However, $CuInS_2$ nanocrystals have not previously been reported for their potential electrocatalytic activity, which promotes reactions between S^{2-}/S_n^{2-} redox couples in QDSSCs.

In the literature, it is well-documented that chalcopyrite Cu−In−S semiconductor compounds possess tremendous structural tolerance for nonstoichiometric variations and exhibit abundant

Received: September 11, 2014
Accepted: November 24, 2014
Published: November 24, 2014

intrinsic defects, which consequently affect their crystalline-phase and physicochemical properties.[27−32] By adjusting the stoichiometric ratio of the Cu/In precursors, this distinction enables Cu−In−S semiconductor compounds to potentially generate high-quality quantum dots (QDs) with an enhanced quantum yield for better emission. For example, Uehara and co-workers have reported pioneering work on improving the photoluminescence intensity of Cu−In−S QDs by introducing Cu deficiencies using nonstoichiometric variation.[27] Liu et al. reported that the concentration of precursors plays a crucial role in determining the emission profile of the $CuInS_2$ and $AgInS_2$ QDs.[30] In addition, some successful approaches for synthesizing one-dimensional Cu−In−S heteronanostructures (HSs) have been reported. According to the work of Lu et al., the size and shape of Cu−In−S SCs can also be modulated by the molar ratio of precursors added during the preparation.[33] Choi et al.[34] have utilized a seed-mediated growth mechanism using Cu-oleate and In-oleate complexes in the synthesis of Cu−In−S HSs with acorn, bottle, and larva shapes.

In the present study, we report a facile one-pot approach for generating nonstoichiometric $CuInS_2$ nanocrystals in which all reactants are loaded in the reaction flask. We controllably changed cationic molar ratios to obtain In-rich and Cu-rich $CuInS_2$ nanocrystals (In-CIS and Cu-CIS), which demonstrated photon-harvesting ability and electrocatalytic activity, respectively, in a QDSSC system. Using Cu-CIS HSs as the CE, an In-CIS/CdS cosensitized solar cell showed improved conversion efficiencies as high as 2.37% under standard AM 1.5 sunlight illumination, which, compared with conventional Pt CEs, represented a 24.7% improvement in efficiency. Both the electrochemical impedance spectroscopy (EIS) data and Tafel polarization confirmed that Cu-CIS-based electrodes exhibited much higher catalytic activity for polysulfide reduction and lower charge-transfer resistance, which supported the enhanced photovoltaic performance. Furthermore, DSSCs fabricated with Cu-CIS CEs also exhibited promising photovoltaic characteristics with an energy-conversion efficiency of 6.11%.

2. EXPERIMENTAL SECTION

Preparation of Nonstoichiometric $CuInS_2$ Nanocrystals. All syntheses were performed under an inert atmosphere using a Schlenk technique.

Cu-CIS HSs were synthesized using the following procedure. In this procedure, 0.6 mmol of copper acetate (97%, Aldrich), 0.2 mmol of indium acetate (99.99%, Alfa Aesar), and 2.5 mL of 1-dodecanethiol (98%, Acros) were dissolved in 5 mL of 1-octadecene (90% Acros) and heated to 40 °C with gentle stirring; this mixture was simultaneously flushed with Ar for 20 min to remove O_2 and residual water. The resulting solution was subsequently placed under the protection of an argon atmosphere and heated to 240 °C for 40 min. The flask was then allowed to naturally cool to room temperature. The undesirable materials were removed by centrifuge at 6000 rpm for 20 min. Afterward, the light yellow supernatant mixture was mixed with a dichloromethane/methanol/acetone mixture (1:2:5, v/v), which was then placed in a centrifuge at 6000 rpm for 5 min. The resulting Cu-CIS HSs were dispersed in hexane for further characterization and experimentation.

In-CIS SCs were synthesized using a synthetic route identical to the process for typical synthesis of Cu-CIS HSs, although the reaction temperature was set to 220 °C for 25 min, and the molar ratio of Cu to In was 1:3. After reaction, 15 mL of chloroform was introduced into the reaction solution, and the solution was spun in a centrifuge at 6000 rpm for 20 min. The resulting supernatant mixture was subsequently mixed with 5 mL of methanol and was then subjected to another round of centrifugation. After discarding the undesirable products, acetone was added to the supernatant to induce In-CIS SC precipitation and was then collected using centrifugation and decantation. In-CIS SCs were finally dispersed in toluene for further characterization and experimentation.

Preparation of SC-Sensitized Photoanodes. The TiO_2-film electrode was prepared according to our previously reported procedure.[19] Briefly, an approximately 4.1 μm thick transparent layer of TiO_2 particles was initially screen printed on the fluorine-doped tin oxide (FTO) glass substrate, and in the next step, an approximately 1.7 μm thick second scattering layer of TiO_2 particles was screen printed. The as-prepared TiO_2 film was annealed at 500 °C for 0.5 h and was subsequently immersed in 2 M 3-mereaptopropionic acid (99%, Alfa-Aesar) in 45 mL of acetonitrile for 24 h. Next, the bare TiO_2-film electrode was sensitized with an In-CIS toluene solution (3 mg/mL) for 24 h in the dark to obtain electrodes stained with In-CIS SCs.

For the first architecture, the above In-CIS-SC-stained electrodes were sequentially immersed into 0.03 M $Zn(CH_3COO)_2$ (99.8%, J. T. Baker) in 50 mL of methanol and into 0.03 M Na_2S (98%, Acros) in a 50 mL water/methanol mixture (3:7, v/v) for 1 min, and the electrodes were rinsed with methanol and dried with nitrogen gas between dips. The above step represents one successive ionic layer adsorption and reaction (SILAR) cycle, and two SILAR cycles were performed for this architecture. The electrode was then subjected to thermal annealing at 250 °C for 3 min. The obtained electrode was characterized as an In-CIS/ZnS-sensitized photoanode.

For the second architecture, the SILAR strategy was employed to immobilize more $CuInS_2$ sensitizers on the presynthesized In-CIS QDs. The above In-CIS-SC-stained electrodes were coated with $CuInS_2$ during four SILAR cycles by sequential dipping into 0.10 M $In(NO_3)_3$ (99.9%, Aldrich) in 50 mL of methanol for 1 min, into 1.25×10^{-3} M $Cu(NO_3)_2$ (98%, Alfa Aesar) in 50 mL of methanol for 0.5 min, and into 0.135-M Na_2S in a 50 mL water/methanol mixture (3:7, v/v) for 4 min. After deposition was complete, the electrodes underwent post-treatment with a ZnS passivation layer in which the electrodes were soaked twice, alternating between 0.03 M $Zn(CH_3COO)_2$ in 50 mL of methanol and 0.03 M Na_2S in a 50 mL water/methanol mixture (3:7, v/v) for 1 min/dip; between dips, the electrodes were rinsed with methanol and dried with nitrogen gas. The electrodes were then subjected to thermal annealing at 250 °C for 3 min. The obtained electrodes were characterized as In-CIS/CIS(4)/ZnS-sensitized photoanodes.

For the third architecture, the SILAR strategy was used to immobilize more CdS sensitizers on the presynthesized In-CIS QDs. The above In-CIS-SC-stained electrodes were deposited with CdS during five SILAR cycles by alternately immersing the electrodes into 0.05 M $Cd(NO_3)_2$ (99%, Hayashi Pure Chemical Ind.) in 50 mL of methanol and into 0.05 M Na_2S in a 50 mL of water/methanol mixture (7:3, v/v) for 1 min/dip. After deposition was complete, the electrodes underwent post-treatment with a ZnS passivation layer. For this treatment, the electrodes were soaked twice, alternating between immersion into 0.03 M $Zn(CH_3COO)_2$ in 50 mL of methanol and into 0.03 M Na_2S in a 50 mL water/methanol mixture (7:3, v/v) for 1 min/dip; the electrodes were rinsed with methanol and dried with nitrogen gas between dips. The electrodes were then subjected to thermal annealing at 250 °C for 3 min. The obtained electrodes were characterized as In-CIS/CdS(5)/ZnS-sensitized photoanodes.

Preparation of Photocathodes. Two types of CEs were produced, as described in the following passage. Cu-CIS HSs (16 mg/mL) were dispersed in hexane and sonicated for 2 h. The resulting solution (40 μL) was spin coated onto the FTO-coated glass substrate. To acquire Cu-CIS-based CEs, the substrates were subsequently heated to 300 °C for 3 min. Pt-based CEs were obtained using DC sputtering equipment (Q150R S, Quorum, USA) at 10 mA and 2×10^{-3} Torr for 5 min.

Assembly of Solar Cell Devices. The above SC-sensitized photoanodes were assembled into sandwich-type cells with different CEs (Cu-CIS-based CEs or Pt-based CEs) using a 60 μm thick Surlyn sheet (DuPont 1702) as a spacer. Using the capillarity effect, the polysulfide electrolyte was then injected into the interelectrode space.

The polysulfide electrolyte contained 1.8 M Na_2S, 2.0 M S (99.98%, Aldrich), and 0.2 M KCl (99%, Acros) in 50 mL of methanol/water (3:7, v/v).

DSSC Fabrication. The DSSCs were fabricated based on the following procedure. The TiO_2 film for the DSSCs was comprised of an approximately 11.9 μm thick transparent layer and an approximately 1.9 μm thick scattering layer, which were prepared using a screen-printing technique. The printed TiO_2 film was annealed at 500 °C and was then soaked in a dye-sensitized solution that contained 0.5 mM Ruthenizer 535-bisTBA dye (N-719, Solaronix) in acetonitrile/*t*-butanol (1:1, v/v) at room temperature for 24 h. The photoanodes and different CEs (Cu-CIS CEs or Pt CEs) were assembled to fabricate sandwich-type cells using a 60 μm thick sealing material (SX1170−60, Solaronix) as a spacer. The I^-/I_3^- electrolyte consisted of 0.1 M lithium iodine (98%, Alfa Aesar), 0.6 M 1-propyl-3-methylimidazolium iodide (99%, UR), 0.1 M guanidinium thiocyanate (99%, Alfa-Aesar), 0.1 M iodine (99.8%, Acros), and 0.5 M 4-*tert*-butylpyridine (96%, Aldrich) in 10 mL of acetonitrile/valeronitrile (85:15, v/v), which was slowly injected into the above cells using the capillary effect.

Characterization. Transmission electron microscopy (TEM) images and high-resolution TEM (HRTEM) images were obtained using a FEI Tecnai G2 F20 microscope (Philips, Holland) with an acceleration voltage of 200 kV. This microscope was equipped with a high-angle annular dark-field (HAADF) detector and an energy-dispersive X-ray spectrometer (EDS). The X-ray diffraction (XRD, Bruker D8 Discover) pattern was conducted for the Cu Kα1 line (λ = 1.54 Å). The surface topography of the as-prepared samples was obtained using atomic force microscopy (AFM) (Shimadzu Co., SPM-9600). The steady-state photoluminescence and UV−visible absorption spectra were measured using JASCO FP-6500 and JASCO V-630 spectrophotometers, respectively. X-ray photoelectron spectroscopy (XPS) was performed using a VG ESCA scientific theta probe spectrometer. The element concentration in the as-prepared samples was determined using an inductively coupled plasma atomic emission spectrophotometer [ICP-AES, JY 2000−2 (Jobin Yvon Horiba)]. Photovoltaic measurements of the solar cell were recorded using a computer-controlled Keithley 2400 source meter under AM 1.5G simulated sunlight (Oriel 6691 450-W Xe arc lamp, CT, USA). The incident photon-to-current conversion efficiency (IPCE) was plotted as a function of wavelength from 300 to 800 nm using a 300 W Xe light source and a monochromator (Peccell Technologies, PEC-S20). Symmetrical dummy cells were employed for both EIS and Tafel polarization using a Zennium electrochemical workstation (Zahner-Elektrik, GmbH & Co KG, Kronach, Germany). The EIS frequency ranged from 100 mHz to 1000 kHz, while the AC magnitude was set at 5 mV. The polarization analysis was conducted at a scan rate of 10 mV s^{-1}.

3. RESULTS AND DISCUSSION

The $CuInS_2$ nanocrystals, which deviated from typical stoichiometry, were synthesized following the protocols we provided in the literature[35] for preparing Cu-based HSs. In summary, a mixture of copper acetate and indium acetate was dissolved in an octadecene solvent containing 1-dodecanethiol, which was used both as the reactant for the sulfur source and as the capping ligands, and the resulting solution was degassed and heated to the desired reaction temperature. The initial Cu/In precursor ratio was influential in determining the shape of the nonstoichiometric $CuInS_2$ nanocrystals. For preparing the In-CIS SCs, the initial concentration ratio of the precursors was [Cu]/[In] = 1:3. Meanwhile, Cu-CIS HSs were synthesized using an identical synthetic method with a 3:1 feed ratio of [Cu]/[In] precursors, and the temperature was increased from 220 to 240 °C. The synthetic strategy for nonstoichiometric $CuInS_2$ SCs is schematically illustrated in Scheme 1.

Scheme 1. Schematic Diagram for the Synthesis of Nonstoichiometric $CuInS_2$ Nanocrystals and Their Application in QDSSCs

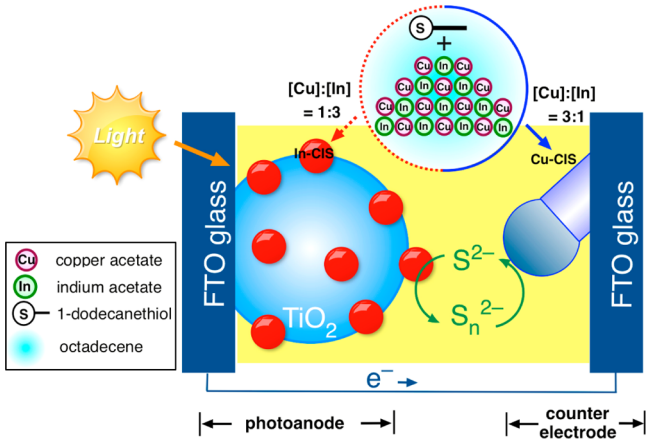

Structure and Morphology Characterization. Figure 1a displays a TEM micrograph of Cu-CIS HSs, which consist of a

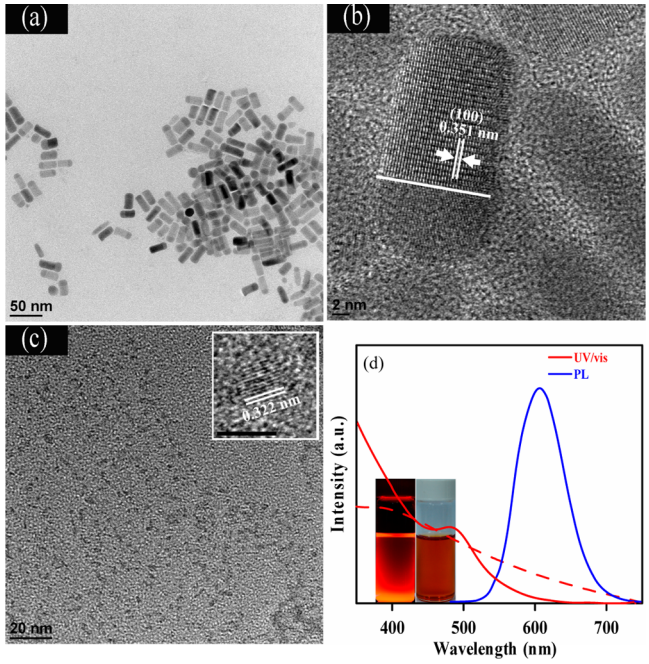

Figure 1. (a) Representative TEM image and (b) HRTEM image of Cu-CIS HSs. (c) TEM image of In-CIS SCs. (inset) HRTEM image of In-CIS SCs. The scale bar in the inset of (c) is 5 nm. (d) UV−vis absorption and emission spectra (λ_{ex} = 430 nm) of In-CIS SCs, as well as the absorption spectrum of the Cu-CIS HSs (no emission is observed). Solid lines are In-CIS data, and red dashed line represents Cu-CIS data. The inset of (d) shows the corresponding photograph of In-CIS SC dispersion in toluene under ambient light (right); the left photograph was taken under irradiation with a hand-held UV lamp.

hemispherical tip and a rodlike body with an average size of ~31 nm (length) × 12 nm (width); these HSs were prepared at a [Cu]/[In] ratio of 3:1. As this figure shows, one end of most Cu-CIS HSs was much darker than the rest of the particle, and this darkening was caused by the high concentration of Cu. The HRTEM image of a single Cu-CIS HS in Figure 1b clearly shows an interface between two different materials within a single rod (the interface is highlighted by a white line), and this

image confirms the presence of two distinct phases within the HS.

This image also exhibits a clear 0.351 nm lattice spacing, which corresponds to the (100) lattice plane of simulated wurtzite $CuInS_2$. HAADF-STEM imaging, in conjunction with EDS elemental mapping and the line-scanning profile (Figure 2), revealed that the hemispherical tip was mainly comprised of

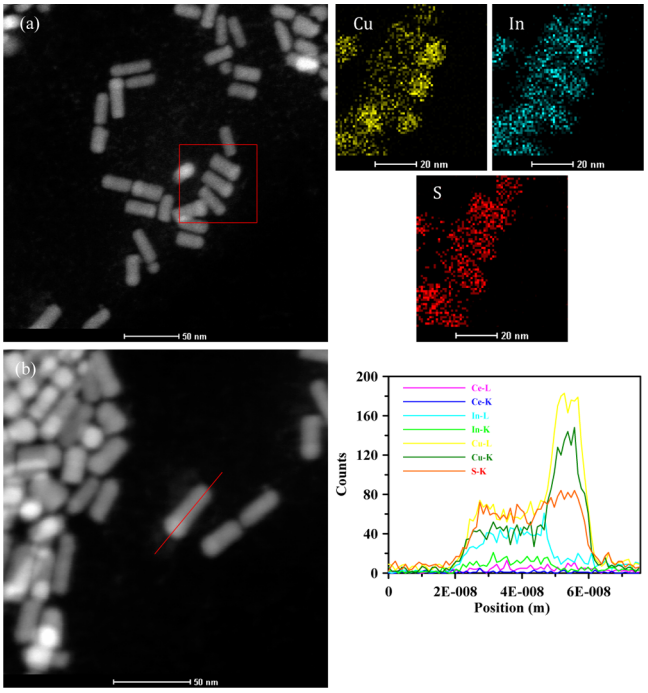

Figure 2. (a) and (b) HAADF-STEM images of Cu-CIS HSs are shown in the left panels. The scale bar is 10 nm. The right panel of (a) is the corresponding elemental mapping of Cu, In, and S elements, as indicated in the left panel (the area marked by the red box). The right panel of (b) is the line profile analysis [the red line in panel (b)] along the Cu-CIS HSs rod's axis. Line profiles of Cu, In, and S were recorded along the line indicated in panel (b). The element Ce was employed as a baseline reference.

Cu and S, while the rodlike body was comprised of Cu, In, and S. As shown in the right panel of Figure 2a, the red signal (the S element) was distributed uniformly throughout the nanorod, while the yellow signal (the Cu element) was located predominately at the head of the HS. Obtained using HAADF-STEM-EDS, Figure 2b reveals line-scanning profiles of an individual Cu-CIS HS; in this figure, the localized Cu and S at the head of the Cu-CIS HS and the distribution of Cu, In, and S throughout the rodlike body of the Cu-CIS HS can be clearly observed. Figure 1c exhibits the typical TEM image of quasi-spherical In-CIS SCs, which were synthesized at the [Cu]/[In] ratio of 1:3 with an average particle size of ~3 ± 0.2 nm. The inset of Figure 1c shows an HRTEM image of representative In-CIS SCs and reveals the well-resolved lattice fringes. The distance between two adjacent planes was 0.322 nm, which corresponds to the (002) lattice plane of chalcopyrite $CuInS_2$. The absorption and photoluminescence spectra of In-CIS SCs and Cu-CIS HSs are shown in Figure 1d. The as-prepared SCs show an exciton absorption peak at 485 nm and an emission peak at 615 nm. Cu-CIS HSs exhibit a broad absorption band and an absorption tail at longer wavelengths in Figure 1d. No emission spectrum from the Cu-CIS HSs was detectable.

The characteristic XRD patterns of the In-CIS SCs exhibited three broad peaks at 2θ values of 26.7°, 46.8°, and 56.2°, which were indexed to diffraction of the (112), (220), and (312) planes, respectively, of chalcopyrite $CuInS_2$, as shown in Supporting Information, Figure S1a. The structure of the as-synthesized Cu-CIS HSs was characterized using XRD, as shown in Supporting Information, Figure S1b. The powder XRD pattern for the Cu-CIS HSs prepared with this method did not match the combined diffraction patterns of chalcopyrite $CuInS_2$ and chalcocite Cu_2S. The diffraction pattern of wurtzite $CuInS_2$ was simulated based on the wurtzite ZnS crystal structure and based on the lattice parameters reported by Kruszynska et al.[36] (space group: $P6_3mc$; unit-cell dimensions: a = 3.906 Å, c = 6.425 Å). XRD measurements verified that two distinct sets of diffraction peaks resulted from wurtzite $CuInS_2$ and chalcocite Cu_2S. For example, three peaks at 22.3°, 26.3°, and 29.8° originated from the (100), (002), and (101) lattice planes, respectively, and these results were very similar to the simulated wurtzite $CuInS_2$ crystal structure. A peak at 37.4° could be indexed to the (102) reflection of the Cu_2S phase. This result also agreed with TEM observations, which demonstrated the formation of Cu-CIS HSs.

To further determine the atomic composition of the nonstoichiometric $CuInS_2$ nanocrystals, ICP-AES and EDS analyses were conducted. As shown in Table 1, the Cu/In

Table 1. Cu/In Molar Ratios and Actual Compositions of Cu-CIS and In-CIS Samples, Determined by ICP and EDS

samples	Cu/In feed ratio	ICP ratio	EDS ratio
Cu-CIS	3:1	2.74:1	2.51:1
In-CIS	1:3	1:3.01	1:2.76

atomic ratios for Cu-CIS HSs and In-CIS SCs (obtained using ICP-AES elemental analysis) were approximately 2.74:1 and 1:3.01, respectively, which were in good agreement with the nonstoichiometric compositions of $CuInS_2$ nanocrystals. EDS analysis (presented in Figure S2 in the Supporting Information) confirmed the presence of Cu, In, and S in Cu-CIS HSs and In-CIS SCs, and the chemical composition ratios obtained from EDS spectra were consistent with the ICP-AES results, as shown in Table 1. In addition, the valence states of the Cu, In, and S in nonstoichiometric $CuInS_2$ nanocrystals were determined using XPS and are depicted in Figure 3. All XPS spectra revealed photoelectron peaks corresponding to Cu 2p, In 3d, and S 2p, and their binding energy values were in strong accord with the values reported in the literature.[17] The energy separation for Cu $2p_{3/2}$ and Cu $2p_{1/2}$ was 19.7 eV (or 20 eV), which is consistent with the previously reported value of 19.9 eV. In the 3d orbital, the core split into In $3d_{5/2}$ and In $3d_{3/2}$ peaks with a peak separation of 7.7 eV (or 7.5 eV). The binding energy values obtained for S 2p core levels were curve fitted with a S $2p_{3/2}$-S $2p_{1/2}$ doublet (blue and red lines) with an approximately 1.2 eV energy difference and a 2:1 intensity ratio.

Formation Mechanism for Nonstoichiometric $CuInS_2$. On the basis of the above experimental investigations, the formation mechanism of nonstoichiometric $CuInS_2$ nanocrystals is likely explained as follows (Scheme 2). Typically, two of the consecutive stages during the simplified growth processes of colloidal nanocrystals include: (i) a nucleation event followed by (ii) crystal growth from nuclei with continuous accumu-

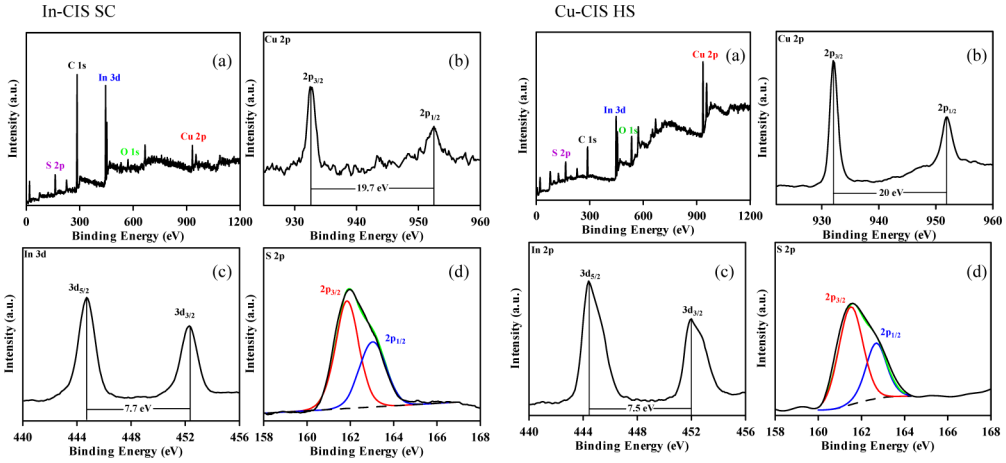

Figure 3. XPS spectra of the as-prepared In-CIS SCs (the left four panels) and Cu-CIS HSs (the right four panels): (a) survey XPS spectrum and core level spectrum for (b) Cu 2p, (c) In 3d, and (d) S 2p. The S 2p spectra were fitted using a convolution of the Gaussian−Lorentzian model. The black line represents raw XPS data; the red and blue lines are Gaussian curve fits at energies corresponding to core atoms; the green line was obtained from the peak sum of red and blue lines; the dashed line is the background signal.

Scheme 2. Schematic Diagram for the Possible Formation Process of Nonstoichiometric $CuInS_2$ Nanocrystals Under Different Initial Cu/In Precursor Ratio

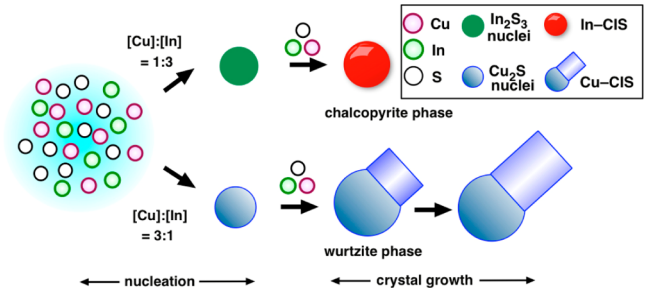

lation of monomers on the nuclei. During the nucleation stage, nuclei formation is initiated as the concentration of monomers becomes sufficiently high (compared with the supersaturation levels). In our case, we postulated that the nucleation stage played a critical role in determining the topology and crystal phases of nonstoichiometric $CuInS_2$ nanocrystals.

As the initial concentration of Cu^+ was much higher than the concentration of In^{3+}, Cu−S monomers preferentially and gradually enriched the solution, and above the critical concentration, the nucleation event suddenly began to generate many Cu_2S nuclei in the form of monomers. Because Cu_2S could nucleate early in the reaction, this progression would benefit wurtzite $CuInS_2$ synthesis because Cu_2S has a hexagonal crystal structure. Furthermore, this compound's S framework was similar to the framework of wurtzite $CuInS_2$, which has packing nearly identical to that of the S sublattices. More importantly, many studies have shown that ionic conductor chalcogenides (e.g., $Cu_{1-x}S$[37−41]) behave in a virtually fluid state, which is caused by their abundant cationic vacancies. This unique feature enables foreign cations to easily dissolve in Cu_2S host nanocrystals, which results in the heteroepitaxial growth of a second phase. Consequently, during the formation of Cu-CIS HSs, Cu_2S nanocrystals were generated at the initial stages and then behaved as both seeds and catalysts for the attachment of $CuInS_2$; these nanocrystals crystallized gradually to form one-dimensional growth of wurtzite HSs. This proposed mechanism can be understood because of the difficulty of forming $CuInS_2$ with a wurtzite structure. It is generally known that $CuInS_2$ exhibits three types of crystal phases: chalcopyrite, zinc-blende, and wurtzite structures. In the chalcopyrite structure, Cu and In atoms are orderly located in the cation sublattice positions, which leads to tetrahedral symmetry. In contrast, zinc-blend and wurtzite $CuInS_2$ structures have a random distribution of Cu and In atoms over the lattice's cation sites, which results in cubic and hexagonal symmetry, respectively. However, wurtzite $CuInS_2$ is a metastable phase and is very difficult to synthesize directly in solution at mild temperatures. Therefore, we suspected that wurtzite $CuInS_2$ formation deposited the pre-existing Cu_2S nuclei in our system.

Under [In]-rich conditions, however, more In precursors could preferentially react with 1-dodecanethiol, and predominantly In_2S_3 nuclei were formed in the initial reaction stage. When the reaction proceeded, dissolved Cu^+ was progressively coordinated with the S atoms that were exposed on the surface of In_2S_3 nuclei; consequently, In-CIS SCs with chalcopyrite structures were obtained.

If equimolar ratios of Cu and In precursors were adopted for the reaction, In_2S_3 nuclei would also form preferentially before the formation of Cu_2S nuclei because the solubility product constant of In_2S_3 ($K_{sp} = 5.7 \times 10^{-74}$) is much smaller than the solubility product constant of Cu_2S ($K_{sp} = 1.6 \times 10^{-48}$). In particular, the formation of In_2S_3 nuclei would require a much lower concentration of In−S monomers than Cu_2S nuclei in the solution. Because the absence of Cu_2S nuclei occurred in the early nucleation stage, the growth of wurtzite $CuInS_2$ could not catalyze deposition on the pre-existing Cu_2S nuclei. This finding led us to consider the possibility that chalcopyrite $CuInS_2$ SC features with emission properties could still be synthesized under a nominal Cu/In ratio of 1:1. To verify this assumption, we compared the optical performance of $CuInS_2$ SCs with different molar ratios of Cu and In precursors. Supporting Information, Figure S3 clearly shows that the emission peak position did not considerably change when the Cu/In ratio varied. However, no explicit absorption peak was observed for the Cu/In ratio of 1:1, but the first excitonic absorption peak of the as-prepared samples became gradually pronounced as the relative concentration of In precursors in the solution increased. As discussed in a previous study,[42] the appearance of this peak reveals a relative minimization of

dx.doi.org/10.1021/am5061992 | ACS Appl. Mater. Interfaces 2014, 6, 22272−22281

intrinsic point defect states exhibited in these I–III–VI-group QDs because the high concentration of In precursors should diminish the abundant Cu vacancies in the I–III–VI-group QDs. Moreover, the XRD patterns of $CuInS_2$ SCs with a 1:1 stoichiometric ratio of Cu and In (shown in Supporting Information, Figure S4) revealed the chalcopyrite structure of $CuInS_2$, but no characteristic peaks from wurtzite $CuInS_2$ or chalcocite Cu_2S appeared. ICP-AES demonstrated that the as-prepared sample had a [Cu]/[In] precursor ratio of 1:1 and indicated a Cu/In ratio of 1:1.2.

Photovoltaic Performance of the Cell Devices. Supporting Information, Figure S5 reveals the temporal evolution of the absorbance spectra of In-CIS SC. With longer reaction time, the absorbance peaks exhibited a gradual red shift to lower photon energy region because of the effect of reduced quantum confinement with increasing particle size. The quantum confinement of electron and hole in In-CIS SC facilitate ultrafast charge separation rate, offering In-CIS possibly being a light-harvesting material in QDSSCs. Cu-CIS HS did not exhibit the quantum confinement effects because its size is much bigger than the Bohr exciton radius (~4 nm) of the bulk $CuInS_2$.[43] However, Cu-CIS HS has good electrocatalytic activity for the reduction of S_n^{2-} to S^{2-} compared with In-CIS SC, as will be discussed below (Electrochemical Behaviors). To evaluate the photovoltaic characteristics of nonstoichiometric $CuInS_2$ SCs, the solar cells were assembled into a sandwich-type configuration when the as-prepared In-CIS SCs and Cu-CIS HSs were employed as light-harvesting sensitizers and CEs, respectively, as depicted in Scheme 1. For comparison, $CuInS_2$ SCs with the initial feed [Cu]/[In] of 1:1 was also employed as light-harvesting sensitizers in QDSSC. Figure 4a shows the current density–voltage (J–V) characteristics of the QDSSCs based on different sensitizers and CEs under simulated AM 1.5G full sunlight intensity, and the summary of photovoltaic parameters is presented in Table 2. It is seen from Table 2 that the QDSSC assembled with sample S0 phothoanode showed cell efficiency of 0.2%. Sample S1 exhibited improved performance, with V_{OC} = 0.57 V, J_{SC} = 5.61 mA cm^{-2}, and fill factor (FF) = 0.31, which yielded a power conversion efficiency (PCE) of 0.98%. AFM confirmed that the TiO_2 surface was coated with several In-CIS SCs, as shown in Supporting Information, Figure S6. Compare with sample S0 photoanode, the higher J_{SC} for the cell with sample S1 photoanode is due to increased injection of charge carriers. As discussed above, In-CIS SCs exhibited a relative minimization of intrinsic point defect states, which would avoid vanishing charge carriers via recombination and/or trapping at the defect location.

To further enhance cell efficiency, the SILAR process was used to enable the deposition of more sensitizers on the preformed In-CIS SCs, which resulted in TiO_2 films with high surface coverage of sensitizing QDs. Figure 4 shows sample S3 with a light-harvesting photoanode that produced a J_{SC} of 7.30 mA cm^{-2}, a V_{OC} of 0.54 V, and an FF of 0.39, which yielded a PCE of 1.54%.

The enhanced J_{SC} can be understood as a result of the increased amount of $CuInS_2$ loaded by the SILAR process, which led to higher light harvesting and an increased amount of electrons being injected into the TiO_2 film. Moreover, Table 2 shows that the photovoltaic performance of sample S5 was significantly improved when additional QD sensitizers were changed from $CuInS_2$ to CdS after SILAR cycles were applied five times. On the basis of previous studies,[18] we know that the

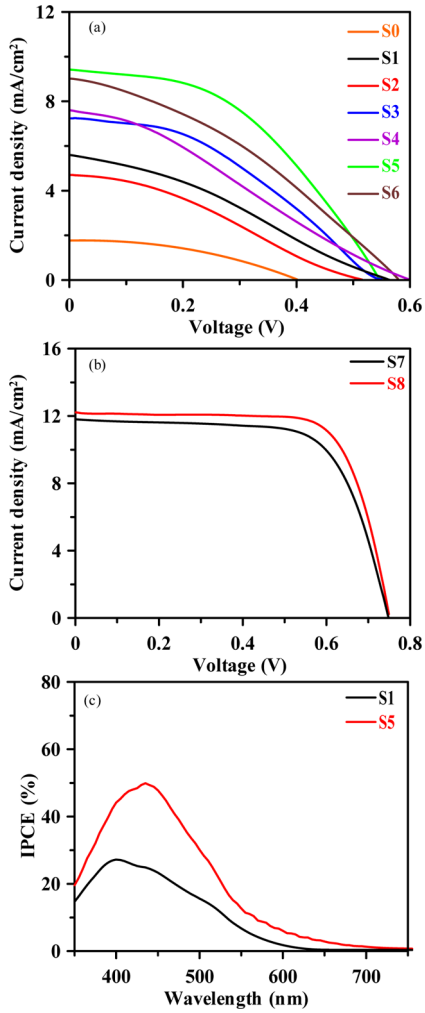

Figure 4. Comparison of J–V curves for (a) QDSSCs and (b) DSSCs prepared under various sensitization conditions and tested under standard global AM 1.5 irradiation. (c) IPCE curves of a QDSSC assembled with the photoanode from sample S1 or S5.

band position created a cascade energy-gap structure when $CuInS_2$ and CdS attached to each other, as shown in Supporting Information, Figure S7. Therefore, the higher J_{SC} of sample S5 most likely resulted from the combined synergetic effects of enhanced light-harvesting capacity and a favorable stepwise cascade. This result agreed well with the IPCE spectra, as shown in Figure 4c. For example, the IPCE profile of sample S1 was 27% at 410 nm. Conversely, the maximum IPCE observed for sample S5 was ~50% at 450 nm, and its response tail extended to 750 nm or more, which, compared with sample S1, was in good agreement with the enhanced J_{SC}. For comparison, the J–V curves for the cell featuring a Pt CE were also recorded and are shown in Figure 4a. The results indicated that the QDSSCs employing Cu-CIS CEs (samples S1, S3, and S5) all generated higher PCEs than the QDSSCs that employed Pt CEs (samples S2, S4, and S6); this finding resulted mainly because of these samples' higher J_{SC} value. The J_{SC} increase was attributed to the higher catalytic ability for the reduction of polysulfide redox species in Cu-CIS CEs than in Pt CEs.

To gain insight into the different catalytic activity of Cu-CIS HS, we also employed N719 and I^-/I_3^- as alternative sensitizers and redox couples, respectively. The DSSCs with Cu-CIS- and Pt-based CEs were fabricated under identical conditions. The

Table 2. Photovoltaic Parameters for Various Solar Cells Fabricated with Different Photoanodes and CEs and the Fitted Impedance Parameters Extracted from Fabricated Symmetric Cells

sample	photoanode	CE	J_{SC} (mA cm^{-2})	V_{OC} (mV)	FF	PCE (%)
S0	$CuInS_2$/ZnS	Cu−CIS	1.79	0.40	0.41	0.30
S1	In−CIS/ZnS	Cu−CIS	5.61	0.57	0.31	0.98
S2	In−CIS/ZnS	Pt	4.72	0.52	0.32	0.78
S3	In−CIS/CIS(4)/ZnS	Cu−CIS	7.30	0.54	0.39	1.54
S4	In−CIS/CIS(4)/ZnS	Pt	7.24	0.60	0.27	1.29
S5	In−CIS/CdS(5)/ZnS	Cu−CIS	9.28	0.57	0.45	2.37
S6	In−CIS/CdS(5)/ZnS	Pt	9.08	0.58	0.36	1.90
S7	N719	Cu−CIS	11.81	0.75	0.69	6.11
S8	N719	Pt	12.61	0.73	0.68	6.32

obtained $J-V$ characteristic curves are shown in Figure 4b, and the main photovoltaic parameters are summarized in Table 2. DSSCs that employed Cu-CIS HSs as CEs had a J_{SC} value of 11.81 mA cm^{-2}, a V_{OC} value of 0.75 V, and an FF value of 0.69, which resulted in efficiencies of 6.11% (compared with the 6.32% efficiency of DSSCs fabricated using Pt as the CE). The results indicated that the Cu-CIS HS also had good catalytic activity suitable for the I^-/I^{3-} electrolyte. Similar electrocatalytic performance of Cu-based metal sulfides HSs has been previously reported by Yi et al. for DSSCs using $CuInS_2$−ZnS HSs as CE materials.[44] According to their report, they noted that an HS with a large aspect ratio could facilitate the catalytic activity of the I_3^-/I^- redox couple and possessed higher electron mobility because of the one-dimensional structure. To further evaluate the effect of a Cu-CIS HS's length in determining photovoltaic performance, Cu-CIS HSs with different lengths were used as CEs. The Cu-CIS HSs were obtained at 240 °C for various reaction times. The growth process of Cu-CIS HSs was monitored with TEM measurements (Supporting Information, Figure S8) to determine the formation evolution of HSs as a function of reaction time. It can be seen that reaction time affected the length of Cu-CIS HSs, but the diameter of Cu-CIS HSs showed a much weaker time dependence. Figure 5 shows the $J-V$ characteristics of

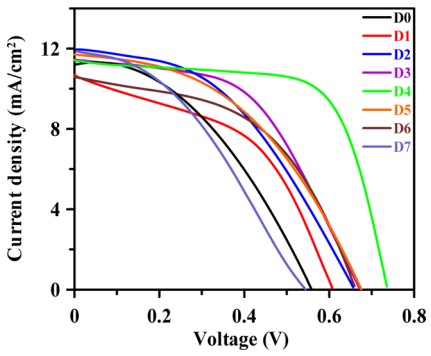

Figure 5. Comparison of $J-V$ curves for DSSCs prepared with various CEs and tested under standard global AM 1.5 irradiation.

DSSCs based on various Cu-CIS CEs under simulated sunlight (AM 1.5G, 100 mW cm^{-2}). As shown in Figure 5 and Table 3, by utilizing a Cu-CIS40 HS as a CE, the conversion efficiency of a DSSC enhanced as the length of the Cu-CIS HSs increased and reached a maximum value. For comparison, Cu_2S nanocrystals were prepared with the same procedure applied to Cu-CIS HSs, although no indium acetate precursors were involved. In Supporting Information, Figure S9, TEM images show that the as-obtained Cu_2S nanocrystals appear nearly

Table 3. Photovoltaic Parameters for DSSCs Fabricated with Different CEs

sample	photoanode	CE[a]	J_{SC} (mA cm^{-2})	V_{OC} (mV)	FF	PCE (%)
D0	N719	Cu-CIS0	11.39	0.60	0.40	2.73
D1	N719	Cu-CIS10	10.57	0.61	0.48	3.12
D2	N719	Cu-CIS20	12.15	0.66	0.44	3.52
D3	N719	Cu-CIS30	11.36	0.67	0.52	4.02
D4	N719	Cu-CIS40	11.38	0.73	0.69	5.80
D5	N719	Cu-CIS50	11.87	0.68	0.44	3.57
D6	N719	Cu-CIS60	10.64	0.67	0.50	3.54
D7	N719	Cu_2S	11.91	0.54	0.38	2.46

[a]The Cu-CIS HSs were obtained at 240°C for 0, 10, 20, 30, 40, 50, and 60 min, and these HSs were identified as Cu-CIS0, Cu-CIS10, Cu-CIS20, Cu-CIS30, Cu-CIS40, Cu-CIS50, and Cu-CIS60, respectively.

spherical. Cu_2S-based CEs in DSSCs were investigated under the same conditions and achieved a PCE of only 2.46%, as shown in Figure 5. Therefore, the above findings indicated that the superior electrocatalytic properties of a Cu-CIS HS in the reduction of the I_3^-/I^- redox couple resulted from its length dependence and novel architectures.

Electrochemical Behaviors. EIS is a steady-state method for examining the interfacial resistances and electron transport properties within an electrochemical system. Figure 6a show the Nyquist plots obtained from the EIS measurement at frequencies ranging from 100 mHz to 1000 kHz. By fitting the results to a suitable equivalent circuit model [as shown in Figure 6b], we determined that the equivalent circuit consisted of the series resistance associated with the catalyst layer that covered the FTO substrate (R_s), the charge transport resistance at the CE-electrolyte (R_{ct}), the constant phase element (CPE) at the CE-electrolyte interface, and the Warburg diffusion resistance (Z_w) of the redox couple in the electrolyte, as listed in Table 4. The R_{ct} of the Cu-CIS CEs (15.9 Ω) was lower than the value for the Pt CEs (257 Ω). The small value of R_{ct} for the Cu-CIS electrode suggested higher electrocatalytic activity for the reduction of S_n^{2-} to S^{2-} in the cells. Indeed, the enhancement of the catalytic activity was directly reflected in the $J-V$ performance of QDSSCs by increasing J_{SC}, as shown in the $J-V$ curves (Figure 4). For comparison purposes, EIS analysis was performed for In-CIS-based electrode (see the Supporting Information, Figure S10a). In-CIS CEs give an unsatisfactory R_c value compare to Cu-CIS- and Pt-based

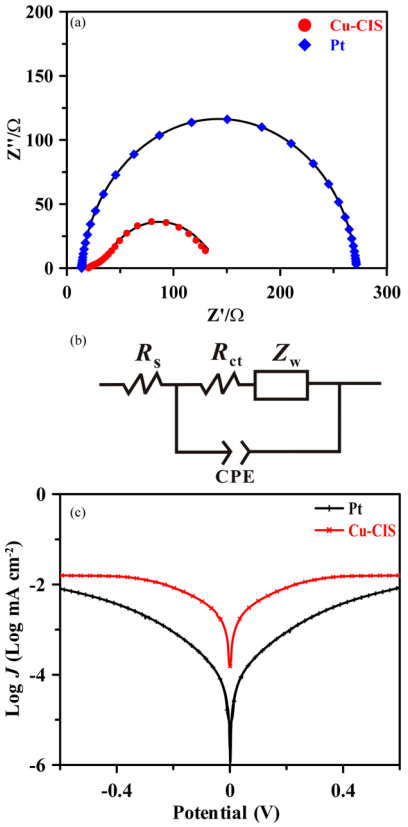

Figure 6. (a) Nyquist (impedance) plots of symmetrical dummy cells (CE/electrolyte/CE) fabricated with two identical Cu-CIS- or Pt-based CEs containing S^{2-}/S_n^{2-} electrolytes. Z′ and Z″are the virtual and real impedances, respectively. Symbols are experimental data, and solid lines represent fitting results. (b) The equivalent circuit of the dummy cells that was used to fit the impedance data. (c) Tafel polarization curves for symmetrical cells fabricated with two identical CEs containing S^{2-}/S_n^{2-}electrolytes.

Table 4. Electrochemical Parameters of the Symmetrical Cells Assembled with Two Identical CEs

CE	R_s (Ω)	R_{ct} (Ω)	CPE (μF)	Z_w (Ω)
Cu-CIS	18.8	15.9	10.9	281
Pt	13.8	257	23.8	*a*

[a]Not determined.

electrodes. The results indicated that In-CIS SCs exhibit poor electrocatalytic activity for the polysulfide reduction.

To gain insight into the charge-transfer properties of electrodes interfaced with various electrolytes, Tafel polarization was measured in symmetrical dummy cells with Cu-CIS- and Pt-based electrodes that were equipped with a S^{2-}/S_n^{2-} redox couple. Figure 6c shows the logarithmic current density (log J) as a function of the voltage (V) for the oxidation/reduction of the redox couple. In the Tafel zone, the exchange current density (J_0) can be calculated from the intercept of the extrapolated linear region of the cathodic branches of the corresponding Tafel plots. From Figure 6c, compared with the Pt-based electrode, the Cu-CIS-based electrode equipped with the S^{2-}/S_n^{2-} electrolyte had a large value of J_0, which suggested higher electrocatalytic activity and lower charge-transfer resistance at the electrolyte-electrode interface. In a comparison study, In-CIS CEs exhibit lowest value of J_0 among the three CEs (Supporting Information, Figure S10b). The results are consistent with the EIS spectra [Figure 6a] because J_0 is inversely proportional to R_{ct}, as given by the following equation:

$$J_0 = \frac{RT}{nFR_{ct}} \quad (1)$$

,where R is the gas constant, T is the temperature, F is the Faraday constant, and n is the number of electrons exchanged in the reaction between the electrolyte and the CE interface.

Moreover, the Tafel polarization curves contain the information about the limiting current density (J_{lim}), which is the intersection between the cathodic branch and the y-axis. On the basis of eq 2, J_{lim} was directly proportional to the diffusion coefficient (D) of the redox couple, as expressed by the equation

$$D = \frac{\delta}{2nFC} J_{lim} \quad (2)$$

,where D is the diffusion coefficient for the redox couple, δ is the spacer thickness between electrodes in a dummy cell, and C is the concentration of the redox couple.

As shown in Figure 6c, the Cu-CIS-based electrode had a large value of J_{lim}, which suggested a small value of Z_w and a large diffusion coefficient (compared with a Pt-based electrode in a S^{2-}/S_n^{2-} redox couple).

4. CONCLUSIONS

In conclusion, a simple one-pot method was developed to prepare nonstoichiometric $CuInS_2$ nanocrystals by mixing the cationic and anionic precursors in an octadecene solvent without complicated precursor preparation, and synthesis was accomplished in a one-pot reaction. As compared with other approaches, this strategy is a straightforward fabrication that can be readily conducted by directly mixing the precursors and capping agent in an octadecene solvent, and synthesis can be accomplished in a one-pot reaction. The results indicated that Cu-CIS HSs were generated when [Cu]/[In] = 3 in the reaction solution. Meanwhile, In-CIS SCs were obtained when [Cu]/[In] = 0.33 in the reaction solution. With the assistance of novel Cu-CIS architecture, which served as the CE, In-CIS/CdS-sensitized solar cells exhibited very promising photovoltaic characteristics, with J_{SC} = 9.28 mA cm^{-2}, V_{OC} = 0.57 V, and FF = 0.45; these cells achieved a PCE of 2.37% (AM1.5G, 100 mW cm^{-2}), which was 24.7% higher than the PCE of QDSSCs fabricated with a Pt-based CE. To the best of our knowledge, this study represents the first report of a QDSSC assembled with $CuInS_2$-based nanocrystals that served as the light-harvesting sensitizer and the CE. According to the EIS and Tafel polarization results, compared with the Pt catalyst, the Cu-CIS HSs exhibited higher catalytic activity for the polysulfide electrolyte system. Moreover, this study describes Cu-CIS HSs that exhibit excellent electrocatalytic activity in QDSSCs, and this study also demonstrates a potential alternative CE in DSSCs that use an I^-/I_3^- electrolyte; consequently, these DSSCs achieved a PCE of 6.11%, which was ∼96% of the PCE for equivalent devices assembled with a Pt CE (6.32%). In addition, the synthetic approaches and possible growth scheme are described and proposed, which might open new perspectives for the controllable synthesis of other copper-based metal chalcogenide nanostructures. Such nanostructures will find many applications in photocatalysis and photovoltaics.

■ ASSOCIATED CONTENT

Supporting Information

TEM images, XRD patterns, and EDS spectra of the as-prepared samples; absorption and photoluminescence spectra of $CuInS_2$ SCs; AFM images of a TiO_2 film coated with In-CIS SCs; the relative band positions of TiO_2, $CuInS_2$, and CdS; and Nyquist plots/Tafel polarization curves of In-CIS. This material is available free of charge via the Internet at http://pubs.acs.org.

■ AUTHOR INFORMATION

Corresponding Author

*E-mail: jychang@mail.ntust.edu.tw. Phone: +886-2-27303636. Fax: +886-2-27376644.

Notes

The authors declare no competing financial interest.

■ ACKNOWLEDGMENTS

The authors thank the Ministry of Science and Technology of the Republic of China for financially supporting this research under Contract No. 102-2628-M-011-001-MY3.

■ REFERENCES

(1) Beard, M. C.; Midgett, A. G.; Hanna, M. C.; Luther, J. M.; Hughes, B. K.; Nozik, A. J. Comparing Multiple Exciton Generation in Quantum Dots To Impact Ionization in Bulk Semiconductors: Implications for Enhancement of Solar Energy Conversion. *Nano Lett.* **2010**, *10*, 3019−3027.

(2) Pijpers, J. J. H.; Ulbricht, R.; Tielrooij, K. J.; Osherov, A.; Golan, Y.; Delerue, C.; Allan, G.; Bonn, M. Assessment of Carrier-Multiplication Efficiency in Bulk PbSe and PbS. *Nat. Phys.* **2009**, *5*, 811−814.

(3) McGuire, J. A.; Sykora, M.; Joo, J.; Pietryga, J. M.; Klimov, V. I. Apparent Versus True Carrier Multiplication Yields in Semiconductor Nanocrystals. *Nano Lett.* **2010**, *10*, 2049−2057.

(4) Shockley, W.; Queisser, H. J. Detailed Balance Limit of Efficiency of p-n Junction Solar Cells. *J. Appl. Phys.* **1961**, *32*, 510−519.

(5) Nozik, A. J. Quantum Dot Solar Cells. *Physica E* **2002**, *14*, 115−120.

(6) Lee, H. J.; Bang, J.; Park, J.; Kim, S.; Park, S.-M. Multilayered Semiconductor (CdS/CdSe/ZnS)-Sensitized TiO_2 Mesoporous Solar Cells: All Prepared by Successive Ionic Layer Adsorption and Reaction Processes. *Chem. Mater.* **2010**, *22*, 5636−5643.

(7) Hossain, M. A.; Jennings, J. R.; Koh, Z. Y.; Wang, Q. Carrier Generation and Collection in CdS/CdSe-Sensitized SnO_2 Solar Cells Exhibiting Unprecedented Photocurrent Densities. *ACS Nano* **2011**, *5*, 3172−3181.

(8) Santra, P. K.; Kamat, P. V. Mn-Doped Quantum Dot Sensitized Solar Cells: A Strategy to Boost Efficiency over 5%. *J. Am. Chem. Soc.* **2012**, *134*, 2508−2511.

(9) Santra, P. K.; Kamat, P. V. Tandem-Layered Quantum Dot Solar Cells: Tuning the Photovoltaic Response with Luminescent Ternary Cadmium Chalcogenides. *J. Am. Chem. Soc.* **2013**, *135*, 877−885.

(10) Benehkohal, N. P.; Gonzalez-Pedro, V.; Boix, P. P.; Chavhan, S.; Tena-Zaera, R.; Demopoulos, G. P.; Mora-Sero, I. Colloidal PbS and PbSeS Quantum Dot Sensitized Solar Cells Prepared by Electrophoretic Deposition. *J. Phys. Chem. C* **2012**, *116*, 16391−16397.

(11) Guijarro, N.; Lana-Villarreal, T.; Lutz, T.; Haque, S. A.; Gomez, R. Sensitization of TiO_2 with PbSe Quantum Dots by SILAR: How Mercaptophenol Improves Charge Separation. *J. Phys. Chem. Lett.* **2012**, *3*, 3367−3372.

(12) Yu, X.; Zhu, J.; Zhang, Y.; Weng, J.; Hu, L.; Dai, S. $SnSe_2$ Quantum Dot Sensitized Solar Cells Prepared Employing Molecular Metal Chalcogenide as Precursors. *Chem. Commun.* **2012**, *48*, 3324−3326.

(13) Heo, J. H.; Im, S. H.; H. Kim, J.; Boix, P. P.; Lee, S. J.; Seok, S. I.; Mora-Sero, I.; Bisquert, J. Sb_2S_3-Sensitized Photoelectrochemical Cells: Open Circuit Voltage Enhancement through the Introduction of Poly-3-hexylthiophene Interlayer. *J. Phys. Chem. C* **2012**, *116*, 20717−20721.

(14) Li, T. L.; Lee, Y. L.; Teng, H. High-Performance Quantum Dot-Sensitized Solar Cells Based on Sensitization with $CuInS_2$ Quantum Dots/CdS Heterostructure. *Energy Environ. Sci.* **2012**, *5*, 5315−5324.

(15) McDaniel, H.; Fuke, N.; Pietryga, J. M.; Klimov, V. I. Engineered $CuInSe_xS_{2-x}$ Quantum Dots for Sensitized Solar Cells. *J. Phys. Chem. Lett.* **2013**, *4*, 355−361.

(16) Luo, J.; Wei, H.; Huang, Q.; Hu, X.; Zhao, H.; Yu, R.; Li, D.; Luo, Y.; Meng, Q. Highly Efficient Core−Shell $CuInS_2$−Mn Doped CdS Quantum Dot Sensitized Solar. Cells. *Chem. Commun.* **2013**, *49*, 3881−3883.

(17) Chang, J.-Y.; Su, L.-F.; Li, C.-H.; Chang, C.-C.; Lin, J.-M. Efficient "Green" Quantum Dot-Sensitized Solar Cells Based on Cu_2S−$CuInS_2$−ZnSe Architecture. *Chem. Commun.* **2012**, *48*, 4848−4850.

(18) Chang, J.-Y.; Lin, J.-M.; Su, L.-F.; Chang, C.-F. Improved Performance of $CuInS_2$ Quantum Dot-Sensitized Solar Cells Based on a Multilayered Architecture. *ACS Appl. Mater. Interfaces* **2013**, *5*, 8740−8752.

(19) Chang, C.-C.; Chen, J.-K.; Chen, C.-P.; Yang, C.-H.; Chang, J.-Y. Synthesis of Eco-Friendly $CuInS_2$ Quantum Dot-Sensitized Solar Cells by a Combined Ex Situ/in Situ Growth Approach. *ACS Appl. Mater. Interfaces* **2013**, *5*, 11296−11306.

(20) Hodes, G.; Manassen, J.; Cahen, D. Electrocatalytic Electrodes for the Polysulfide Redox System. *J. Electrochem. Soc.* **1980**, *127*, 544−549.

(21) Gonzalez-Pedro, V.; Xu, X.; Mora-Sero, I.; Bisquert, J. Modeling High-Efficiency Quantum Dot Sensitized Solar Cells. *ACS Nano* **2010**, *4*, 5783−5790.

(22) Yang, Z.; Chen, C.-Y.; Liu, C.-W.; Chanh, H.-T. Electrocatalytic Sulfur Electrodes for CdS/CdSe Quantum Dot-Sensitized Solar Cells. *Chem. Commun.* **2010**, *46*, 5485−5487.

(23) Radich, J. G.; Dwyer, R.; Kamat, P. V. Cu_2S Reduced Graphene Oxide Composite for High-Efficiency Quantum Dot Solar Cells. Overcoming the Redox Limitations of S^{2-}/S_n^{2-} at the Counter Electrode. *J. Phys. Chem. Lett.* **2011**, *2*, 2453−2460.

(24) Xu, J.; Yang, X.; Wong, T.-L.; Lee, C.-S. Large-Scale Synthesis of Cu_2SnS_3 and $Cu_{1.8}S$ Hierarchical Microspheres as Efficient Counter Electrode Materials for Quantum Dot Sensitized Solar Cells. *Nanoscale* **2012**, *4*, 6537−6542.

(25) Zu, J.; Yang, X.; Yang, Q.-D.; Wong, T.-L.; Lee, C.-S. Cu_2ZnSnS_4 Hierarchical Microspheres as an Effective Counter Electrode Material for Quantum Dot Sensitized Solar Cells. *J. Phys. Chem. C* **2012**, *116*, 19718−19723.

(26) Zhang, H.; Cheng, K.; Hou, Y. M.; Fang, Z.; Pan, Z. X.; Wu, W. J.; Hua, J. L.; Zhang, X. H. Efficient CdSe Quantum Dot-Sensitized Solar Cells Prepared by A Postsynthesis Assembly Approach. *Chem. Commun.* **2012**, *48*, 11235−11237.

(27) Uehara, M.; Watanabe, K.; Tajiri, Y.; Nakamura, H.; Maeda, H. Synthesis of $CuInS_2$ Fluorescent Nanocrystals and Enhancement of Fluorescence by Controlling Crystal Defect. *J. Chem. Phys.* **2008**, *129*, 134709.

(28) Nam, D.-E.; Song, W.-S.; Yang, H. Noninjection, One-Pot Synthesis of Cu-Deficient $CuInS_2$/ZnS Core/Shell Quantum Dots and Their Fluorescent Properties. *J. Colloid Interface Sci.* **2011**, *361*, 491−496.

(29) Kim, Y.-K.; Ahn, S.-H.; Chung, K.; Cho, Y.-S.; Choi, C.-J. The Photoluminescence of $CuInS_2$ Nanocrystals: Effect of Non-Stoichiometry and Surface Modification. *J. Mater. Chem.* **2012**, *22*, 1516−1520.

(30) Liu, L.; Hu, R.; Law, W.-C.; Roy, I.; Zhu, J.; Ye, L.; Hu, S.; Zhang, X.; Yong, K.-T. Optimizing the Synthesis of Red- and Near-Infrared $CuInS_2$ and $AgInS_2$ Semiconductor Nanocrystals for Bioimaging. *Analyst* **2013**, *138*, 6144−6153.

(31) Zhong, H.; Bai, Z.; Zou, B. Tuning the Luminescence Properties of Colloidal I−III−VI Semiconductor Nanocrystals for Optoelec-

tronics and Biotechnology Applications. *J. Phys. Chem. Lett.* **2012**, *3*, 3167−3175.
(32) Torimoto, T.; Kameyama, T.; Kuwabata, S. Photofunctional Materials Fabricated with Chalcopyrite-Type Semiconductor Nanoparticles Composed of $AgInS_2$ and Its Solid Solutions. *J. Phys. Chem. Lett.* **2014**, *5*, 336−347.
(33) Lu, X.; Zhuang, Z.; Peng, Q.; Li, Y. Controlled Synthesis of Wurtzite $CuInS_2$ Nanocrystals and Their Side-by-Side Nanorod Assemblies. *CrystEngComm* **2011**, *13*, 4039−4045.
(34) Choi, S.-H.; Kim, E.-G.; Hyeon, T. One-Pot Synthesis of Copper−Indium Sulfide Nanocrystal Heterostructures with Acorn, Bottle, and Larva Shapes. *J. Am. Chem. Soc.* **2006**, *128*, 2520−2521.
(35) Chang, J.-Y.; Cheng, C.-Y. Facile One-Pot Synthesis of Copper Sulfide−Metal Chalcogenide Anisotropic Heteronanostructures in A Noncoordinating Solvent. *Chem. Commun.* **2011**, *47*, 9089−9091.
(36) Kruszynska, M.; Borchert, H.; Parisi, J.; Kolny-Olesiak, J. Synthesis and Shape Control of $CuInS_2$ Nanoparticles. *J. Am. Chem. Soc.* **2010**, *132*, 15976−15986.
(37) Zhuang, T.-T.; Fan, F.-J.; Gong, M.; Yu, S.-H. $Cu_{1.94}S$ Nanocrystal Seed Mediated Solution-Phase Growth of Unique Cu_2S−PbS Heteronanostructures. *Chem. Commun.* **2012**, *48*, 9762−9764.
(38) Han, S. K.; Gong, M.; Yao, H. B.; Wang, Z. M.; Yu, S. H. One-Pot Controlled Synthesis of Hexagonal-Prismatic $Cu_{1.94}S$-ZnS, $Cu_{1.94}S$-ZnS-$Cu_{1.94}S$, and $Cu_{1.94}S$-ZnS-$Cu_{1.94}S$-ZnS-$Cu_{1.94}S$ Heteronanostructures. *Angew. Chem., Int. Ed.* **2012**, *51*, 6365−6368.
(39) Regulacio, M. D.; Ye, C.; Lim, S. H.; Bosman, M.; Polavarapu, L.; Koh, W. L.; Zhang, J.; Xu, Q. H.; Han, M. H. One-Pot Synthesis of $Cu_{1.94}S$−CdS and $Cu_{1.94}S$−$Zn_xCd_{1-x}S$ Nanodisk Heterostructures. *J. Am. Chem. Soc.* **2011**, *133*, 2052−2055.
(40) Han, W.; Yi, L.; Zhao, N.; Tang, A.; Gao, M.; Tang, Z. Synthesis and Shape-Tailoring of Copper Sulfide/Indium Sulfide-Based Nanocrystals. *J. Am. Chem. Soc.* **2008**, *130*, 13152−13161.
(41) Wang, J.; Chen, K.; Gong, M.; Xu, B.; Yang, Q. Solution−Solid−Solid Mechanism: Superionic Conductors Catalyze Nanowire Growth. *Nano Lett.* **2013**, *13*, 3996−4000.
(42) Chang, J.-Y.; Wang, G.-Q.; Cheng, C.-Y.; Lin, W.-X.; Hsu, J.-C. Strategies for Photoluminescence Enhancement of $AgInS_2$ Quantum Dots and Their Application as Bioimaging Probes. *J. Mater. Chem.* **2012**, *22*, 10609−10618.
(43) Zhong, H.; Lo, S. S.; Mirkovic, T.; Li, Y.; Ding, Y.; Li, Y.; Scholes, G. D. Noninjection Gram-Scale Synthesis of Monodisperse Pyramidal $CuInS_2$ Nanocrystals and Their Size-Dependent Properties. *ACS Nano* **2010**, *4*, 5253−5262.
(44) Yi, L.; Liu, Y.; Yang, N.; Tang, Z.; Zhao, H.; Ma, G.; Su, Z.; Wang, D. One Dimensional $CuInS_2$−ZnS Heterostructured Nanomaterials as Low-Cost and High-Performance Counter Electrodes of Dye-Sensitized Solar Cells. *Energy Environ. Sci.* **2013**, *6*, 835−840.